Preprint Cambridge Centre for Computational Chemical Engineering ISSN 1473 – 4273

Optical band gap of cross-linked, curved, and radical polyaromatic hydrocarbons

Angiras Menon [1,4], Jochen A.H. Dreyer [1], Jacob W. Martin [1,4] Jethro Akroyd [1], John Robertson [2] and Markus Kraft [1,3,4]

released: 26 April 2019

[1] Department of Chemical Engineering and Biotechnology
University of Cambridge
West Site
Philippa Fawcett Drive
Cambridge, CB3 0AS
United Kingdom
E-mail: mk306@cam.ac.uk

[2] Department of Engineering
University of Cambridge
JJ Thomson Avenue
CB3 0FA Cambridge
United Kingdom

[3] School of Chemical and Biomedical Engineering
Nanyang Technological University
62 Nanyang Drive
Singapore, 637459

[4] Cambridge Centre for Advanced Research and Education in Singapore (CARES)
CREATE Tower
1 Create Way
Singapore, 138602

Preprint No. 225

Keywords: band gap, crosslinked aromatics, buckybowl, curved PAH, polar aromatics, fullerene-like

Edited by
Computational Modelling Group
Department of Chemical Engineering and Biotechnology
University of Cambridge
West Site, Philippa Fawcett Drive
Cambridge, CB3 0AS
United Kingdom

Fax: + 44 (0)1223 334796
E-Mail: c4e@cam.ac.uk
World Wide Web: http://como.cheng.cam.ac.uk/

Abstract

In this work, the optical band gaps of polycyclic aromatic hydrocarbons (PAHs) crosslinked via an aliphatic bond, curved via pentagon integration and with radical character were computed using time-dependent density functional theory. A variety of different functionals were benchmarked against optical band gaps (OBGs) measured by ultraviolet-visible spectroscopy with HSE06 being most accurate with a percentage error of 6% for a moderate basis set. Pericondensed aromatics with different symmetries were calculated with this improved functional providing new scaling relationships for the OBG versus size. Further calculations showed crosslinks cause a small decrease in the OBG of the monomers which saturates after 3–4 crosslinks. Curvature in PAHs was shown to increase the optical band gap due to the resulting change in hybridisation of the system, but this increase saturated at larger sizes. The increase in OBG between a flat PAH and a strained curved one was shown to be equivalent to a difference of several rings in size for pericondensed aromatic systems. The effect of σ-radicals on the optical band gap was also shown to be negligible, however, π-radicals were found to decrease the band gap by $\sim$0.5 eV. These findings have applications in understanding the molecular species involved in soot formation.

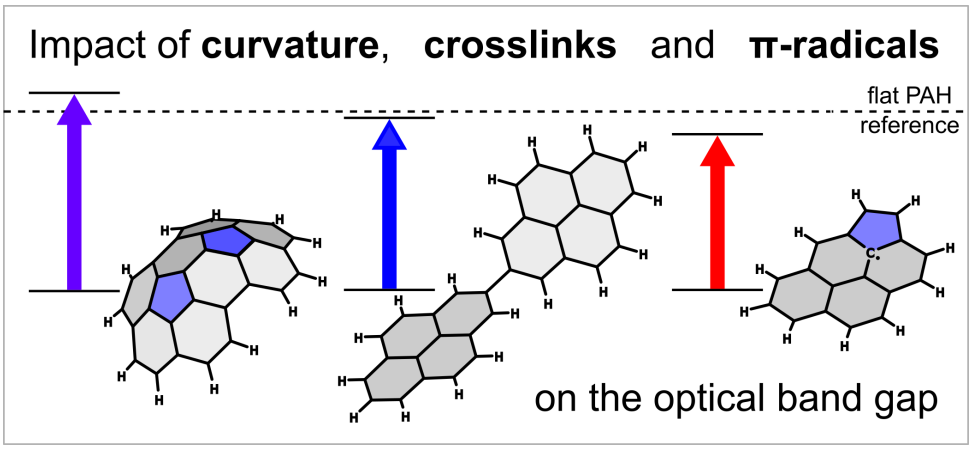

Highlights

- Time-Dependent Density Functional Theory was used to compute the optical band gap of polycyclic aromatic hydrocarbons calibrated against experimental UV/Visible spectroscopy.
- The impact of PAH size, symmetry, curvature, cross-linking, and radicals on their optical band gap was computed and interpreted in the context of understanding optical measurements in sooting flames.

Contents

1 Introduction

Polycyclic aromatic hydrocarbons (PAHs) are hydrogen terminated graphene fragments ubiquitous in nature with a rich chemistry. A delocalised π-bonding network stabilises these pericondensed aromatics making them the thermodynamically preferred arrangement for hydrocarbons [49]. This stability makes them ubiquitous in thermal processes such as in interstellar dust [50], the moon Titan's atmosphere [32, 58] and terrestrial combustion [20]. Their rich chemistry has also attracted interest for molecular electronics with a variety of graphene ribbons synthesized and different schemes for tuning their electronic structure have been proposed [19]. Crosslinking via aliphatic bonds as well as integrating topological defects such as pentagonal rings are two such schemes for tuning the electronic properties that have not received much theoretical study to date. An example for PAHs curved by pentagon integration is their potential in battery applications, as they have been shown to store large amounts of lithium [56].

Our main interest is the role of PAHs as precursors for carbonaceous particulates in flames. A fundamental understanding of this process is of great interest, be it for mitigating emissions from combustion or for the commercial production of carbonaceous particles for applications such as tire filler materials, dyes, paints, and molecular electronics [8]. Such an understanding requires insight into both the gas-phase chemistry and particle dynamics. While there are detailed descriptions of particle processes there is still a lack of knowledge regarding particle inception, where gas phase species first form soot nuclei [52, 54]. Once the PAHs have reached a sufficient size they condense, but the exact size and structure of these nucleating PAHs is still unknown. Inception is frequently modelled as dimerisation of moderate PAHs such as pyrene and coronene. However, molecular dynamics studies suggest that the bulk melting points of moderate PAH clusters are too low to form soot at flame temperatures [12, 28, 51]. The difficulty of modelling inception and gas-phase chemistry necessitates the use of diagnostic techniques to help determine what PAHs may be involved in particulate formation.

One property of particular interest for PAHs is the optical band gap (OBG). Previous studies reported the OBG at different positions within flames by using laser extinction and the Tauc method [26]. Minutolo *et al.* assumed an indirect electron transition and observed a range of OBGs in their benzene/air flames depending on whether the flame was non-sooting (3 eV – 4.6 eV), nearly-sooting (1 eV – 5 eV) or sooting (0.6 eV – 1 eV) [3]. Adkins and Miller performed a similar study on a diluted ethylene/N_2/air flame but found a much smaller OBG range of 1.85 – 2.35 eV while assuming that the extinction corresponded to a direct transition [17]. A similar OBG range of 1.7 – 2.4 eV was found by Botero *et al.* for sooting n-heptane/toluene flames, again assuming a direct transition [41].

Once the OBGs inside a flame are known, the challenge is to correlate the measured values to specific PAH structures present in both soot and the gas phase. Soot consists of stacked PAHs as confirmed by x-ray diffraction studies [2] and Raman analysis [4]. Furthermore, Robertson and O'Reilly have found that sp^2 carbon systems, such as soot, have their electronic properties governed by $\pi - \pi^*$ interactions such as those in PAHs [25]. Therefore, OBGs measured in flames should be indicative of PAHs. There have been several studies on how the OBG is dependent of the number of benzenoid rings in the PAH. Robert-

son and O'Reilly used Hückel molecular orbital theory calculations and showed that the OBG scales with $M^{-\frac{1}{2}}$, where M is the number of aromatic rings in the carbon system for clusters of diamond-like-carbon [25]. Adkins and Miller then performed time-dependent density functional theory (TD-DFT) calculations to obtain the OBG of moderately-sized peri-condensed PAHs in the D_{2h} point group, by approximating the OBG as the energy between the highest occupied molecular orbital (HOMO) and lowest unoccupied molecular orbital (LUMO) transition [17]. These results were correlated to OBG measurements in a diluted ethylene/N_2/air flame, indicating peri-condensed PAHs comprised of 10–20 rings. This is in agreement with simulations performed by Yapp *et al.* on the same flame, using a stochastic population balance model to resolve the PAHs in the gas phase and soot. A OBG profile was calculated based on the obtained PAH compositions, and a comparison to experiments by Botero *et al.* suggested that the smallest peri-condensed PAHs contributing to the OBG consist of 16 rings [41, 53]. However, more complex structures such as curved and cross-linked PAHs as well as PAHs containing aliphatic side-chains might be present in flames. Curved PAHs are hereby caused by strain induced by the integration of internal pentagonal five-member rings [1, 47]. Cross-links are formed by aliphatic bonds between PAHs and, as this results in steric interactions between the rings, also induces non-planarity. In a further study, Adkins and Miller computed the OBG of several hundred PAHs of different topologies, including different benzenoid PAHs, acenes and structures with pentagonal rings. The calculated OBGs of these species were correlated with the number of rings for a more comprehensive OBG taxonomy of PAHs [18]. For the curved PAHs, they found that curvature increases the OBG due to σ interactions, but this was secondary to molecular size effects from the number of rings [18]. A direct quantification of how the curvature impacts the OBG was not made. Reports that include OBGs of cross-linked PAHs are even scarcer. The aforementioned studies were also primarily limited to closed-shell PAHs, whereas there has been recent interest in radical PAHs, especially resonance stabilized or π-radical PAHs and their role in soot formation [29].

Even though the understanding of the correlation between PAH size, structure and OBG has advanced substantially, it was primarily based on computational studies. Previously, TD-DFT calculations have used the B3LYP functional due to its widespread applicability, but the accuracy of B3LYP and other functionals has not been explored for PAHs.

The purpose of this study is twofold. First, experimental UV-visible spectroscopy OBG measurements of a selection of small PAHs are used to evaluate the performance of TD-DFT calculations with different functionals in predicting the OBG of PAHs. The selected experimental test set PAHs have different structures, including cross-links, peri-condensed species, acenes, and species with pentagonal rings, to represent some of the main PAH classes potentially involved in soot formation. The different hybrid functionals were benchmarked against the experimental results to identify the most suitable one. Second, the best performing functional was used to elucidate the effect of various PAH characteristics, such as size and symmetry, cross-linking by aliphatic bond formation, curvature, and radical character on their OBG.

2 Materials and Methods

2.1 Ultraviolet-visible spectroscopy

The optical band gap of 18 different small PAHs and benzene were measured by means of ultraviolet-visible (UV-Vis) spectroscopy. These were chosen to represent a range of structures, namely peri-condensed (benzene to perylene), linear acenes (benzene to tetracene), cross-linked (phenyls) and pentagon-containing PAHs (fluorene and acenaphthylene).

UV-Vis absorption spectra of PAHs dissolved in cyclohexane were recorded. Cyclohexane was chosen as it is transparent in the wavelength range of interest, is capable of dissolving PAHs and is expected to cause minimal solute-solvent interactions as it is non-polar. PAH concentrations of 10^{-5}-10^{-4} M were used to minimise PAH-PAH interactions and to keep the maximum absorbance below 1.5 AU. The solution was placed in a quartz cuvette with 1 cm path-length and the sample's UV-Vis spectra were measured between 200-800 nm (Agilent, Cary 8453) using a step size of 0.5 nm with 0.5 s per step. The optical band gap was determined from plots of absorbance vs wavelength using the absorption edge method [11]. This method has found wide use in optical characterisation of organic thin films by UV-Vis spectroscopy, such as in Costa *et al.* [14]. Further details of this method are found in the supplementary material.

2.2 Time-Dependent Density Functional Theory

Optimised geometries of the PAHs were determined using the 6-311G(d,p) basis set and the B3LYP hybrid functional. This combination has been shown to provide accurate molecular geometries in other works [42]. TD-DFT calculations were then performed on these geometries using the same 6-311G(d,p) basis set and different hybrid exchange-correlation functionals. This included widely used hybrid functionals with exact exchange (HSE06, B3LYP, B971, PBE0, and B972), functionals including long-range interaction parameters and dispersion corrections (CAM-B3LYP and ω-B97xD) and the Minnesota functional M06. The initial test calculations were performed on naphthalene, biphenyl and fluorene to identify the most suitable functional. These were chosen to cover the flat, cross-linked and pentagonal categories and are economic enough for timely TD-DFT calculations. The accuracy of the different functionals was quantified by comparing the percentage error between the computed ($E_{\mathrm{g,DFT}}$) and experimental OBG ($E_{\mathrm{g,Exp}}$):

$$P.E. = \frac{E_{\mathrm{g,DFT}} - E_{\mathrm{g,Exp}}}{E_{\mathrm{g,Exp}}}. \tag{1}$$

Once the best functional was identified, the OGBs of some larger, cross-linked and curved PAHs were also calculated. The cross-linked PAHs consisted of naphthalene, pyrene, coronene and ovalene monomer units connected by aliphatic bonds in para-geometries. To investigate the effect of curvature, constrained geometry optimisations were performed on corannulene, a small, curved molecule with a central pentagonal ring and five outer hexagonal rings. The constrained geometry optimisation fixed the value of the dihedral angles

between the pentagonal plane of corannulene and the hexagons beneath, thereby varying the curvature of the corannulene molecule. This is explained further in the supplementary material. All DFT calculations were performed using Gaussian09 (Gaussian Inc.) [39] except for the corannulene geometry optimisations, which were performed using Gaussian03 [40] to use the constrained geometry optimisation implemented in this version of the program. The Gaussian09 calculations were performed in parallel on 20 Intel Xeon cores using 32 GB of memory. The Gaussian03 calculations were performed using the Darwin Supercomputer of the University of Cambridge High Performance Computing Service (http://www.hpc.cam.ac.uk/).

3 Results and discussion

3.1 Choice of functional

In order to quantify the accuracy of the considered TD-DFT functionals, the percentage errors (PE) between simulated and measured OBGs was calculated for three representative PAHs (naphthalene, biphenyl and fluorene) (Fig.1). All functionals overpredict the OBG of the three PAHs when compared to the experiments. The simulated OBG of naphthalene is more accurate than that of biphenyl and fluorene. All functionals predict a larger OBG for fluorene than for naphthalene, whereas the measured OBG is 4.2 eV for naphthalene and 4.1 eV for fluorene. This indicates that the B3LYP/6-311G(d,p) level of theory used for the geometry optimisation might be less accurate for the complex non-planar structures of the cross-linked biphenyl and five-ring containing fluorene. Amongst the considered functionals, HSE06 results in the most accurate OBGs with an average P.E. of 6%. This is supported by a similar DFT study performed on semiconductors [13]. The next best performing functional is the widely used B3LYP with an average PE of 20%. Functionals such as the CAM-B3LYP and ω-B97xD overestimate the OBG significantly. The reason for this is that they are parametrised to give orbital energies for accurately calculating the transport gap, which includes the energy to create an unbound electron-hole pair, rather than the OBGs [45]. The computed OBG values are also in agreement with the current literature. For example, the OBG of 4.85 eV for naphthalene predicted using B3LYP and the 6-311G(d,p) basis set is very similar to the 4.75 eV reported for B3LYP and the similar 6-31+G(d,p) basis set [14].

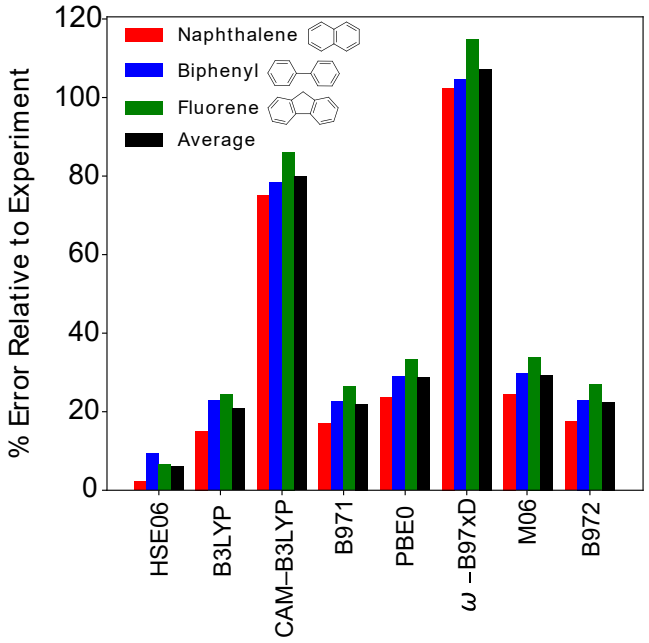

Figure 1: *Comparison of the percentage errors between the OBGs obtained from experimental UV-Vis absorption experiments and TD-DFT simulations using different Hybrid Functionals. Also shown are the structures of the three test PAHs.*

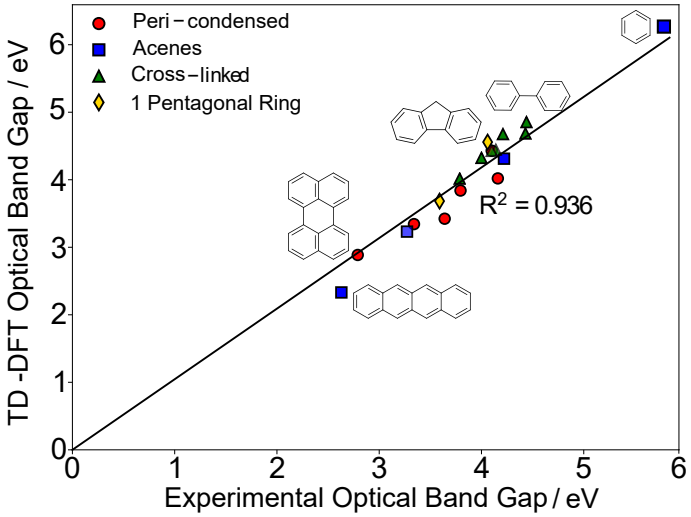

Figure 2: *Comparison between the optical band gaps obtained from TD-DFT simulations and UV-Vis absorption measurements of 19 different PAHs. Also shown are the molecule structures of some representative PAHs.*

The experimental OBGs of 18 PAHs and benzene were compared to the TD-DFT predictions obtained with the most accurate functional to further evaluate the applicability of

HSE06 for PAH OBG simulations (Fig. 2). Overall, there is good agreement between the simulated and measured OBGs for all PAH geometries considered (see Table S2 for full list). The largest deviation between the computational and experimental OBG is observed for tetracene, at a percentage error of 11 % and absolute error of 0.3 eV. The absolute OBG values are also in good agreement with previous studies. For example, TD-DFT predicts OBGs of 2.89 eV for perylene, 3.84 eV for chrysene and 2.33 eV for tetracene while the semi-emperical ZINDO/S predicted 2.82 eV, 3.86 eV and 2.81 eV respectively [44]. Even though the TD-DFT and semi-empirical OBGs are very similar, semi-empirical methods can struggle with more complex organic structures outside their parametrisation [7]. Therefore, TD-DFT with a combination of the HSE06 functional and 6-311G(d,p) basis set is suitable for OBG calculations of PAHs.

3.2 Trends for Flat PAHs of varying symmetry

With the accuracy of the TD-DFT method shown, the OBGs of additional PAHs were simulated. These included PAHs that are expected to form during hydrocarbon combustion but are difficult to acquire commercially. Previous studies have shown that molecule size, typically quantified by the number of benzenoid rings M, is the determining factor of the optical band gap [18, 25]. The TD-DFT results show that the OBGs of the acenes decrease more rapidly with M than for D_{2h} and D_{6h} peri-condensed PAHs (Fig. 3), which is in agreement with previous reports [18]. The smaller OBG of acenes for a given M can hereby be explained by their Clar structures. They only have one clar sextet, making them electronically more similar to graphene than the peri-condensed PAHs. The correlation between the OBG and M of the three PAH classes follows the reported inverse power law, namely $a \cdot M^{-1/2}+b$ [25] or $c \cdot M^{d}$ [18], with a, b, c and d being fitting parameters. For D_{2h} peri-condensed PAHs, the current TD-DFT simulations result in $c = 5.621$ and $d = -0.376$, similar to $c = 5.978$ and $d = -0.327$ reported previously [18]. The power-law fit for acenes gives $c = 6.479$ and $d = -0.732$, again similar to $c = 8.913$ and $d = -0.891$ in [18]. The effect of symmetry is also very apparent, with the lowest symmetry group, the C_{2v} acenes possessing substantially lower OBGs than the more symmetric D_{2h} and D_{6h} peri-condensed PAHs. There is also a noticeable difference between the D_{2h} and D_{6h} species, highlighted by the 7-ring D_{6h} coronene having a slightly higher OBG than the much smaller 4-ring D_{2h} pyrene.

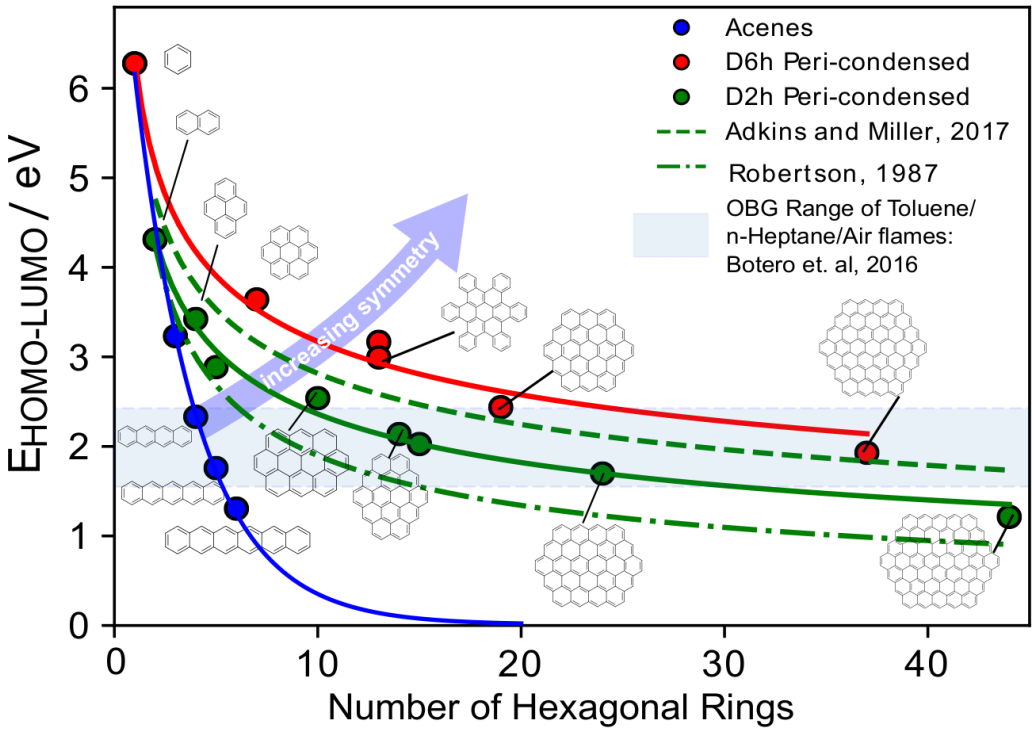

Figure 3: *Plot of the optical band gap of PAHs against number of rings, M. Previous literature results from similar fittings done by Adkins and Miller [18] and Robertson [25] are also shown.*

Figure 3 also gives some indication of which isolated PAHs have OBGs within the range of those observed in flames for the different symmetry groups. For D_{2h} peri-condensed species, the flame region of OBGs includes isolated PAHs with 14-24 rings. For D_{6h} peri-condensed species, the reported OBG range in flames correlates to approx. 19-20 rings (the size of circumcoronene) and extends well past circumcircumcoronene (37 rings) to species containing hundreds of rings. However, the latter are likely larger than what can be expected to form in a flame from HRTEM studies [41]. For acenes, the flame region of OBGs includes isolated PAHs only 4–5 rings in size. It should also be noted that PAH clusters have OBGs approximately 1 eV lower than their isolated counterparts [16]. Thus for a given OBG measured inside the flame, the PAH size that can be assigned to it decreases if a PAH cluster was measured. Acene clusters are therefore unlikely because the constituting PAHs would be too small to form a condensed phase in a flame and are not thermally stable [15, 51]. However, species such as ovalene (D_{6h} peri-condensed) and hexabenzocoronene (D_{2h} peri-condensed) might be large enough to incept and their clusters would result in OBGs similar to what was measured in flames.

3.3 Trends for cross-linked PAHs

The variation in OBG for flat PAHs is well known in the literature. Less is known about the effect of cross-linking on the OBG of PAHs. Cross-linking reactions between PAHs has been observed in flames and hypothesized as a possible route for soot particle inception via chemical clustering [9, 36, 43]. Cross-linking also can be a mechanism of carbonization of soot nanoparticles, as bridge forming between PAHs requires the release of hydrogen from the PAH, thereby increasing the carbon-to-hydrogen ratio. The following calculations aim to probe the effect of such cross-linking reactions on the OBG of complex PAHs. Since the agreement between HSE06/6-311G(d,p) TD-DFT calculations and experiments is good for the smaller cross-linked (supplemental information), the DFT calculations were therefore extended to larger and more complex cross-linked PAHs. The variation in the OBG with increasing number of homogeneous cross-linked PAHs was further studied by performing TD-DFT calculations of naphthalene, pyrene, coronene, and ovalene (Fig. 4a), cross-linked in the para-position, that is forming linear chains. The homogeneous cross-linked structures vary in size from the respective monomer to the octamer for naphthalene, the pentamer for pyrene, and the trimer for coronene and ovalene.

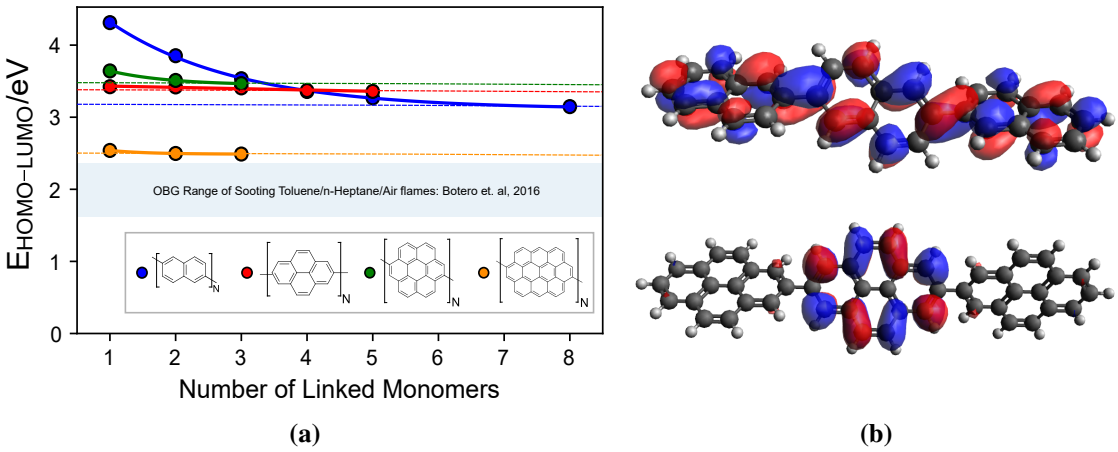

Figure 4: *a) Plot of optical band gap against number of linked monomers for homogeneous aromers. An exponential decay curve has been fitted to guide the eye, with the dashed lines representing the expected asymptotic gap value. b) LUMO orbitals of p-ternaphthyl (top) and p-terpyrenyl (bottom)*

The results suggest that cross-linked structures of moderate PAHs have a reduced OBGs that reach an asymptote. When naphthalene is the repeat unit, there is a significant reduction in the OBG of $\approx$ 1.1 eV for 8 monomers. However, when larger PAHs such as pyrene, coronene, and ovalene are the repeat units, the final reduction of the OBG is only around 0.1 eV. In contrast, previous studies found that clustering by physical agglomeration of PAHs effects a decrease in OBG of approximately 1 eV even for PAHs as large as ovalene, which is not the case here [16]. The observed trends can be explained by considering the change of the relevant orbitals when the monomer size increases. The LUMO of

p-ternaphthyl extends across all three naphthalene units, thus each one contributes to the LUMO energy and consequently the OBG. For p-terpyrenyl, the DFT calculations indicate that the LUMO is localised onto only the central pyrene, and the addition of further pyrene monomers has little influence on its LUMO (Fig. 4b). Similar observations are made for the HOMOs of these two molecules. For larger p-naphthyls, the orbital localization can also be observed. This indicates that the number of monomers required for orbital localization depends on the size of the monomers. Therefore, the localization of orbitals is a function of monomer size and number, explaining the observed asymptotes in Fig. 4a.

It should be noted that the asymptotic OBGs of all cross-linked species are higher than the OBGs observed in ethylene and toluene flames by either Adkins and Miller [17] or Botero *et al.* [41]. This agrees with previous studies for pyrene and coronene that suggested that such clusters are unlikely to be in flames [34] and hence it is understandable that their OBG does not match those measured in flames. However, even for the case of ovalene, the asymptotic OBG is higher than those observed in flames. In contrast, physical clusters of ovalene were seen to have OBGs that are in the range of those observed in such sooting flames [16]. Thus homogeneous chemical clustering by cross-linking would require larger PAH monomers than homogeneous physical clustering to match the observed OBGs in flames.

The effect of cross-linking between different PAHs on the OBG was also explored computationally. Heterogeneous cross-linked structures of naphthalene, pyrene, coronene, and ovalene were chosen in order to use the same monomer PAHs as the homogeneous case:

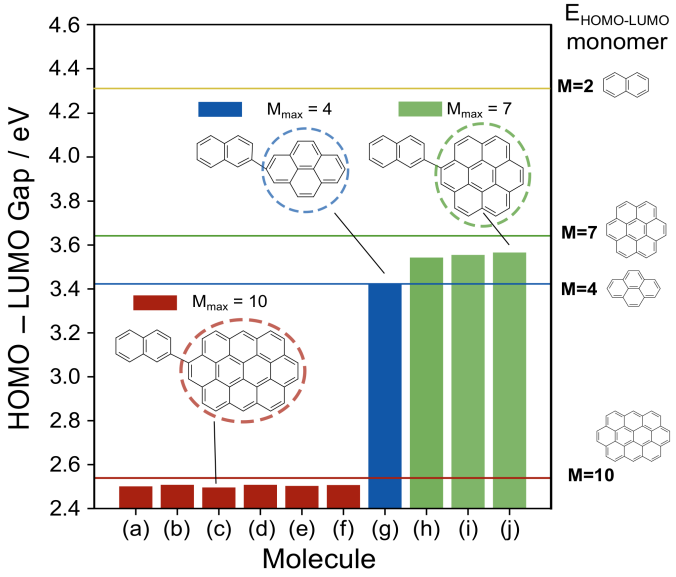

Figure 5: *Optical band gap of cross-linked structures of naphthalene, pyrene, coronene, and ovalene. M_{max} is defined as the number of rings in the largest PAH monomer fragment in the cross-linked PAH (blue for pyrene, green for coronene, red for ovalene). The structures of the PAHs are found in Fig S5 in the supplemental information. The horizontal lines on the bar plot show the optical band gap of the 4 different monomer PAHs for reference.*

Figure 5 would suggest that the optical band gap of heterogeneously cross-linked PAHs is strongly correlated with the optical band gap of the largest monomer PAH fragment within the PAH. In other words, the OBG of the heterogeneously cross-linked PAHs is controlled by the largest PAH/lowest OBG of the monomer PAH fragments in the molecule. This is clearly seen for cross-linked structures between naphthalene and a larger PAH, with species (c), (g), and (j) having OBG values very close to the larger PAH of pyrene, coronene, and ovalene respectively. Similarly, all heterogeneous cross-linked structures which contain ovalene have OBGs very close to ovalene, although there is a slight reduction suggesting that there may be a minute amount of spread of the HOMO and LUMO orbital across the aliphatic cross-link. However, there are complications for PAHs that have coronene as the largest fragment cross-linked to a pyrene fragment. In this case, the OBG of pyrene and coronene are quite close (3.64 and 3.42 eV respectively), and the OBG of the cross-linked PAHs are $\approx$ 3.55 eV, which is nearer to the average of the OBGs of pyrene and coronene. Nevertheless, using the OBG of coronene is still clearly a reasonable approximation for molecules (h), (i), and (j).

In addition to the localization effect in cross-linked PAHs, the formation of a cross-link introduces another degree of freedom in the PAH, namely the rotation of the monomer fragments about the cross-link axis. Tuning of such electronic and optical properties by twisting fragments in a polymer has been seen experimentally, for example in TiO_2 based-dyes for solar cell applications [57]. Particularly at the higher temperatures experienced in flames, it may be the case that a cross-linked PAH will be able to adopt several rotational conformers, resulting in a spread of the OBG. The upper bound of this effect can be seen by considering the rotation of the two phenyl fragments in biphenyl. As the cross-linked PAH with the smallest individual monomer fragments, biphenyl is expected to be able to rotate with the most ease and therefore have the largest spread in its OBG. This effect was explored by means of a relaxed scan of the biphenyl molecule with the dihedral angle of the cross-link bridge used as the scan coordinate. The minimum energy geometry and optical band gap were then determined for each rotational conformer along the scan point.

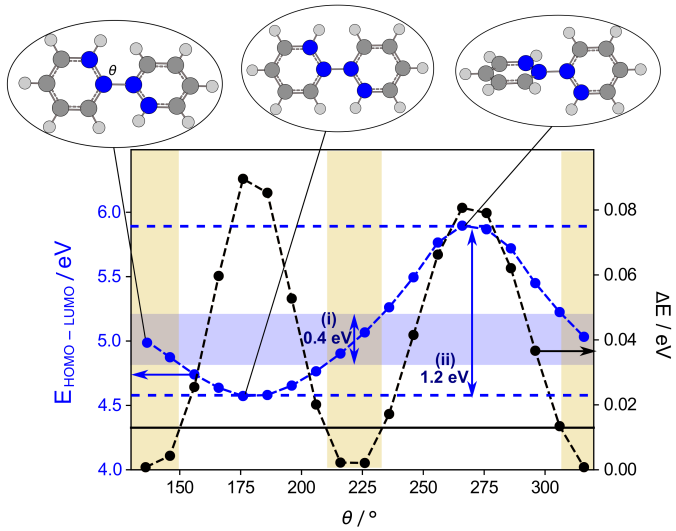

Figure 6: *Optical band gap and change in energy of biphenyl rotational conformers as a function of the dihedral angle, θ. Examples of some of the rotational conformers in the scan are illustrated in the plot, with the atoms comprising the dihedral angle θ highlighted in blue. The beige and blue shaded regions represent the rotational conformers accessible at 298K and their corresponding OBG values.*

Figure 6 suggests that some spread in the OBG is expected for cross-linked PAHs due to their ability to rotate. Rotational conformers are deemed to be accessible if the deviation between the energy of the conformer and that of the equilibrium biphenyl geometry was less than or equal to the Boltzmann thermal energy, k_BT. At 298 K, the regions shaded in beige are accessible to biphenyl, resulting in a modest spread in optical band gap of 0.4 eV. At a temperature of 1500 K, typical of those in flames, all conformers are expected to be accessible, as k_BT has a value of 0.13. Thus, in flame, biphenyl could have an optical band gap spread of 1.3 eV. This spread corresponds to a maximum decrease in the OBG of 0.37 eV compared to biphenyl's equilibrium geometry, and a maximum increase of 0.93 eV. As a result, rotation appears to favor an increase in the OBG over the equilibrium value in the case of biphenyl. This increase in OBG is significant enough that it would have to be considered when making optical measurements at higher temperatures. However, it should also be noted that biphenyl represents the cross-linked PAH that is most likely to rotate. Larger cross-linked PAHs are unlikely to have so many rotational conformers accessible due to the additional energy required, and so the spread in optical band gap expected would be lower. It is also expected that the more cross-links that form, the more difficult it will be for internal rotations about the cross-link to occur, meaning the increase in OBG due to rotation is likely mainly significant for smaller cross-linked PAHs as opposed to those with larger monomers or multiple cross-links.

To summarize, for cross-linking between PAHs, the OBG can be approximated by the OBG of the largest monomer in the system. The rotation of monomer fragments about a cross-link was seen to result in a significant spread in the optical band gap of biphenyl, and resulted in a net increase in the optical band gap of biphenyl when considering all

conformers. However, this was noted to be an upper bound as larger cross-linked PAHs and clusters of such PAHs are expected to require greater energy to effect internal rotation, and so the effect is hypothesized to be significant only for smaller cross-linked PAHs. These results suggest that forming a cluster of PAHs by continuous cross-linking would require larger PAHs present than for physical clustering to explain the lower OBG regimes measured in flames, as there is no additional reduction in OBG due to forming a network of PAHs like there is for physical clustering.

3.4 Trends for curved PAHs

Finally, the effect of pentagons and curvature on the OBG of PAHs is investigated. Curved PAHs form via the integration of interior pentagons into their geometry. This can occur, for example, from zig-zag edge oxidation of a PAH [47]. Understanding how pentagonal rings and curvature affect the OBG is desired, as the presence of pentagonal-ring containing curved PAHs such as fullerene and corannulene has been observed in soot and flames [6] and may contribute to OBG measurements. Therefore, it is useful to understand what sort of pentagonal-ring structures would have OBGs similar to those observed in flames. For example, fluorene and acenaphthylene have quite different OBGs (4.1 and 3.6 eV respectively) despite having similar structures. This can be explained by aromatic differences as Zdetsis and Economou recently found a correlation between aromaticity and OBG [5]. The position of the pentagon is very different in acenaphthylene and fluorene, resulting in them having different Clar sextets. By calculating the aromatic fluctuation index [37] of the rings in both fluorene and acenaphthylene using Multiwfn [35], it is found that the hexagonal rings in fluorene are significantly more aromatic than their counterparts in acenaphthylene, as acenaphthylene has one Clar sextet shared between it's two hexagonal rings. The differences in aromaticity between fluorene and acenaphthylene help explain their difference in OBG.

The comparison between experiments and TD-DFT simulations for fluorene and acenaphthylene indicate that HSE06/6-311G(d,p) gives reasonably accurate OBGs for PAHs containing 5-member rings (Supplemental information). The comparison of these two molecules suggests that slight differences in pentagon position can have significant impacts on aromaticity and the OBG. Such differences are likely to be of even more importance when the PAHs are curved due to internal pentagon integration. For example, a recent study by Martin *et al.* found that more curved PAHs have larger dipole moments due to the π-electron flexoelectric effect. Additionally, by applying strain to corannulene, they found that the dipole moment increased linearly with the pyramidalization angle [31], showing that curvature can have a significant impact on the properties of PAHs. Previous studies have suggested similar ideas, with Adkins *et al.* finding that curvature effects are generally secondary to those of size and shape for larger PAHs [18]. However, it would be useful to establish the optical band gap ranges in which PAH curvature has a significant effect. To do this, the OBG of a set of curved PAH species of varying size, symmetry, and number of pentagons (and therefore curvature) was computed using the same levels of theory as before. This set of PAHs was previously studied by Martin *et al.* to elucidate the effect curvature and size had on dipole moment [31]. This is seen in Figure 7.

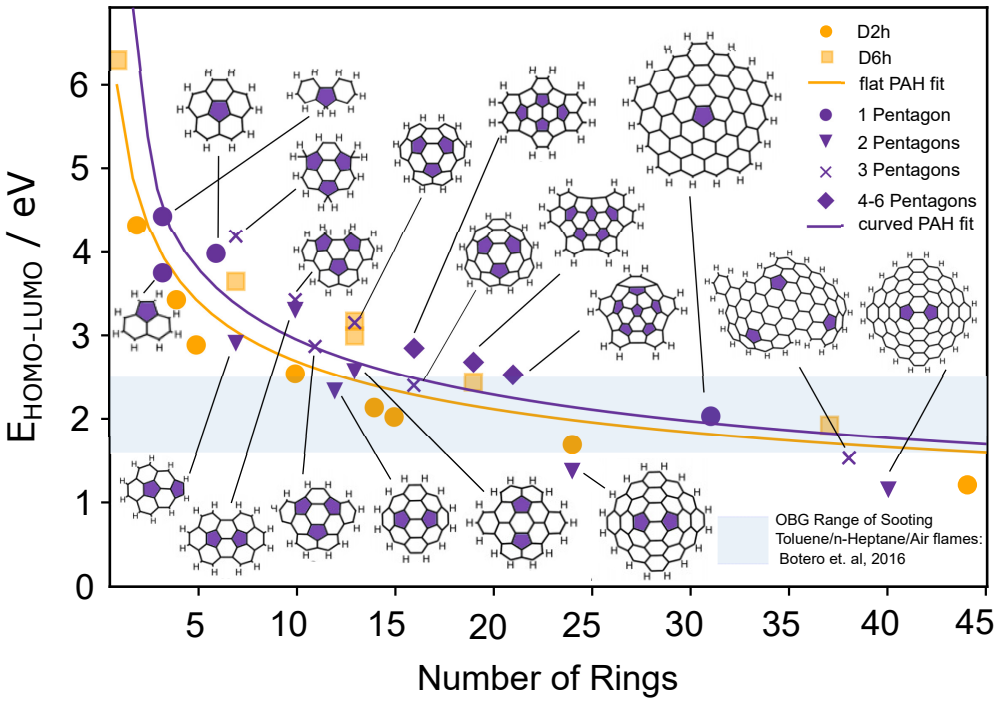

Figure 7: *Optical band gap of curved PAHs with a varying number of rings. The PAHs are numbered according to the number of pentagons they contain. The lines shown are power-law fittings, comparing the fit to all the peri-condensed flat PAHs calculated in section 3.2. The full list of curved PAHs studied can also be found in Fig S6 in the supplemental information.*

Due to the curved PAHs having different number of pentagons, the symmetry of the curved PAHs are quite different. Therefore when comparing to flat peri-condensed PAHs, the power-law fitting in Figure 7 was done for the combined set of D_{2h} and D_{6h} PAHs previously computed in Figure 3. Figure 7 helps establish some guidelines on when the effect of curvature impacts the OBG of peri-condensed PAHs. For smaller PAHs (and therefore higher OBG values), the effect of curvature is important, and arguably of similar significance to the size and symmetry effects. This appears to be the case up until around PAHs of size 15-20 rings. In this smaller PAH range, one can also see that the 2-pentagon PAHs have lower OBGs that are very similar to the D_{2h} flat PAHs. The $\geq$3 pentagon containing curved PAHs can be seen to have OBGs that are similar and even exceeding that of the highly symmetric D_{6h} PAHs in the same size range. As a result, if one takes an OBG of 2.4 eV, corresponding to the upper limit of that measured by Botero *et al.* in flames [41], one can see that a flat peri-condensed PAH would be expected to be around 12–13 rings to give this, whilst a curved PAH would need to be around 16–17 rings to give the same value. Typically, the OBGs measured in flames are related to the size of the peri-condensed species, which led to the conclusion that modest sized PAHs such as ovalene could be present in soot [16, 17]. However, the above analysis suggests the same higher OBG mode could similarly be attributed to curved PAHs of larger sizes which could have increased dispersion interactions. This larger OBG mode in flames is generally attributed to nascent soot as opposed to more mature soot, so the results here

also suggest that consideration of larger curved PAH species may be relevant to nascent soot conditions.

Figure 7 also confirms that the effect of curvature on the OBG is also finite, namely that it becomes less significant as the PAHs get larger. After PAHs grow enough, size is clearly the more important factor impacting OBG. At the lower OBG mode of around 1.7 eV, one would expect the flat and curved PAHs to be of roughly the same size. This would suggest that the decrease in OBG as soot matures cannot be attributed to potential curvature integration after soot formation, but due to other mechanisms, such as growth of PAHs.

To understand why the effect of curvature seems to become less relevant for larger species, it is helpful to consider what happens if curvature is reduced in a PAH by applying strain. For example, by considering the smallest PAH with a fully integrated pentagon, corannulene, and constraining it to have varying degrees of curvature, one can see the variance in optical band gap solely with curvature. To do this, the curvature of corannulene was varied by fixing the value of the dihedral angles during geometry optimisation. The OBG was then calculated as with the other PAHs.

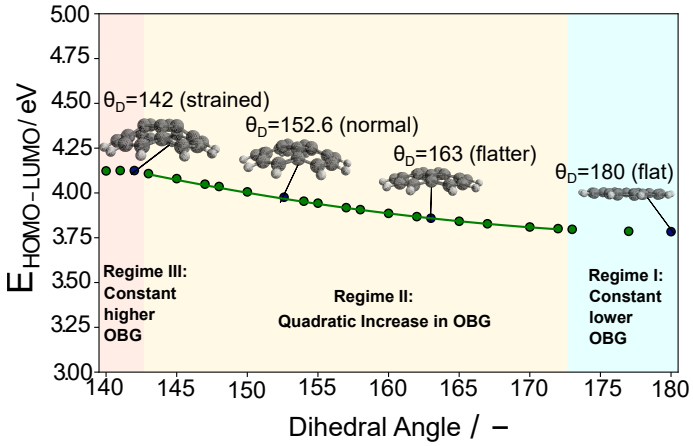

Figure 8: *Plot of the OBG of corannulenes subjected to different amounts of strain.*

Figure 8 shows the variance in the OBG of corannulene as it is subjected to different degrees of strain. Flat corannulene has dominantly π character, and has the lowest optical band gap, which is consistent with smaller flat PAHs having lower band gaps than curved ones. As the corannulene is strained into a curved geometry, its OBG increases as more σ character is introduced into the π-bonding due to the change from sp^2 to sp^3 hybridisation [30, 31]. This agrees with observations made by Jäger *et al.* [27]. Three distinct regimes are seen in Figure 8. The first is for the very flat corannulenes, where the OBG is constant. The dihedral angle needs to reach 175° before an increase in OBG is observed. Then, the OBG increases in a quadratic manner with the dihedral angle, suggesting a reasonably strong dependence on curvature of the OBG. The overall increase in OBG between the flat geometry and the curved saturation geometry is 0.4 eV, which is similar to the difference seen between smaller/moderate flat and curved PAHs in Figure 7. One can also see that once a dihedral angle of around 142° is reached, there is no further change in the OBG, meaning additional curvature no longer increases the optical band gap. The corannulene shows that there is a limit to the amount that curvature impacts the optical band gap in

PAHs, which could also explain why larger curved PAHs have similar optical band gaps to larger flat PAHs. Even though the larger curved PAHs in this case are more curved than corannulene, it would seem that their optical band gap is already saturated by the size of the PAH and adding curvature is less important. For small and moderate PAHs, this is not the case, and adding curvature effects a noticeable change in optical band gap due to the σ-character.

3.5 Trends for open-shell PAHs

3.5.1 σ-radical PAHs

The previous sections considered PAHs of various different geometries, but all structures were closed-shell species, so whether or not there is a difference if the PAH has a radical nature is next explored. Firstly, a single hydrogen was removed from the acene, D_{2h}, and D_{6h} PAHs studied in the first section. The structures of these PAHs can be found in Figure S4 in the supplemental information. This forms an open-shell PAH σ-radical, with one radical site. Such PAHs are of interest as they are formed during the HACA mass growth process [20, 22]. Soot is also known to possess several radical sites on it's surface [24] that have ramifications for surface growth and oxidation processes of such particles as well as PAHs in the gas phase [21, 33]. The effect of radicals on optical properties of PAHs is thus important to take into account. The effect of the radical site and its position in the PAH on the OBG is then compared to the closed-shell counterpart, using the same computational methods as before. This is seen in Figure 9.

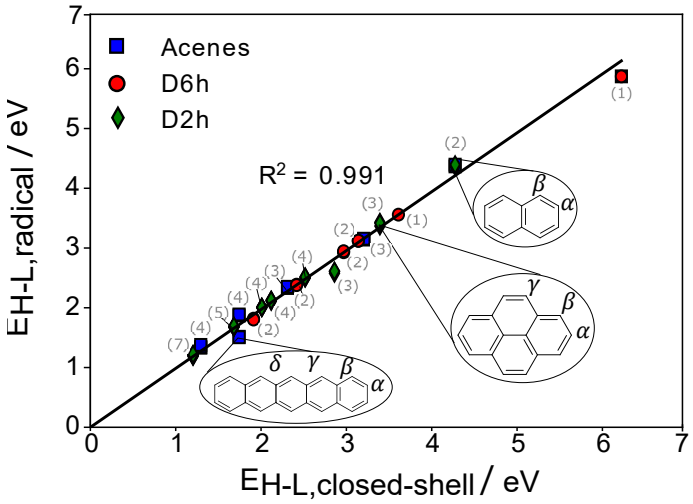

Figure 9: *Comparison between the OBG of open-shell flat PAHs containing one radical site and their closed-shell counterparts. The gray numbers represent the number of unique radical sites the PAH in question possess. Examples are given for naphthalene (2), pyrene (4), and pentacene (5) with each unique potential radical site demarcated with a Greek letter. Other base structures are located in Figure S4 in the supplemental information. The straight line plotted represents the open and closed-shell counterparts having the same OBG.*

Figure 9 suggests that there is almost no difference between the OBG of a single radical site open-shell PAHs and their closed-shell counterparts, as most of the simulated points lie on the $y = x$ line. The position of the radical site on the PAH also seems to have almost no impact, as this would appear on Figure 9 as a scatter of points lying on the same vertical line, but most points for the different radical sites are near indistinguishable. This was due the minimal impact on the HOMO and LUMO energies which are π-orbitals that are orthogonal to the low lying σ-orbitals responsible for the carbon hydrogen bonding. There was a very slight shift towards lower orbital energies for the case of the radical, but this is negligible compared to the magnitude of the HOMO and LUMO energies. The orbital densities make it clear that since removing a hydrogen removes a σ-bond and not a π-bond, the aromatic network of the PAH is conserved, leading to the OBG being invariant to this change. Therefore, it can be stated that the OBG of a σ-radical PAH and it's corresponding closed shell PAH are likely identical.

The one exception to the above rule in the DFT calculations appears to be pentacene, where two distinct points are identified, with one representing the α and β sites and the other representing the γ and δ sites. Strangely, no other acene radicals have this bi-modal OBGs, even the larger hexacene, so it could well be an artifact of the DFT calculation. Nevertheless, the average of the two pentacene radical OBGs is approximately equal to the OBG of closed-shell pentacene. Therefore, the approximation that the OBG of a σ-

radical flat PAH is the same as the closed shell PAH is valid. From a flame diagnostics perspective, this means that OBG measurements in flames could be attributed to either closed or σ open-shell PAHs. Much like how the degree of cross-linking is not reflected in the OBG, neither is the σ radical character of the soot/gas-phase present.

3.5.2 π-radical PAHs

Another key category of PAH species include resonance-stabilized radical (RSR) PAHs such as indenyl RSRs, peri-condensed RSRs, cyclopentamethylene RSRs, and triangulene RSRs. Example RSRs in each of these categories can be found in Figure S7 in the supplemental information. Resonance-stabilized radical species are known to form from reactions of unsaturated hydrocarbons [38], and play important roles in the initial formation chemistry of smaller gas-phase PAHs [48, 58]. Recently, RSR PAHs have been proposed as potential precursors to the formation of soot, initiated first by growth of RSRs by HACA or vinyl addition followed by radical-chain reactions resulting in an incipient soot particle consisting of several RSR and closed-shell PAHs covalently linked [29, 43, 52]. Understanding how the optical band gap of RSR PAHs compares to their closed shell counterparts can help shed light on the differences in properties between these two classes and what this could mean for soot formation. To do so, the OBG of several different classes of RSR PAHs was computed. These include four categories of RSR PAHs. The first is those formed from growth of indenyl which are hypothesized as seed radical for PAHs [29]. The second is the traditional odd-number carbon peri-condensed radicals which have been seen in mass-spectra analyses of PAHs in flames [9, 23]. The third is PAHs containing pentagonal rings and methylene groups, which have been observed in young soot particles by atomic force microscopy [46]. Finally, the fourth category consists of triangulene-like PAHs. This is seen in Figure 10.

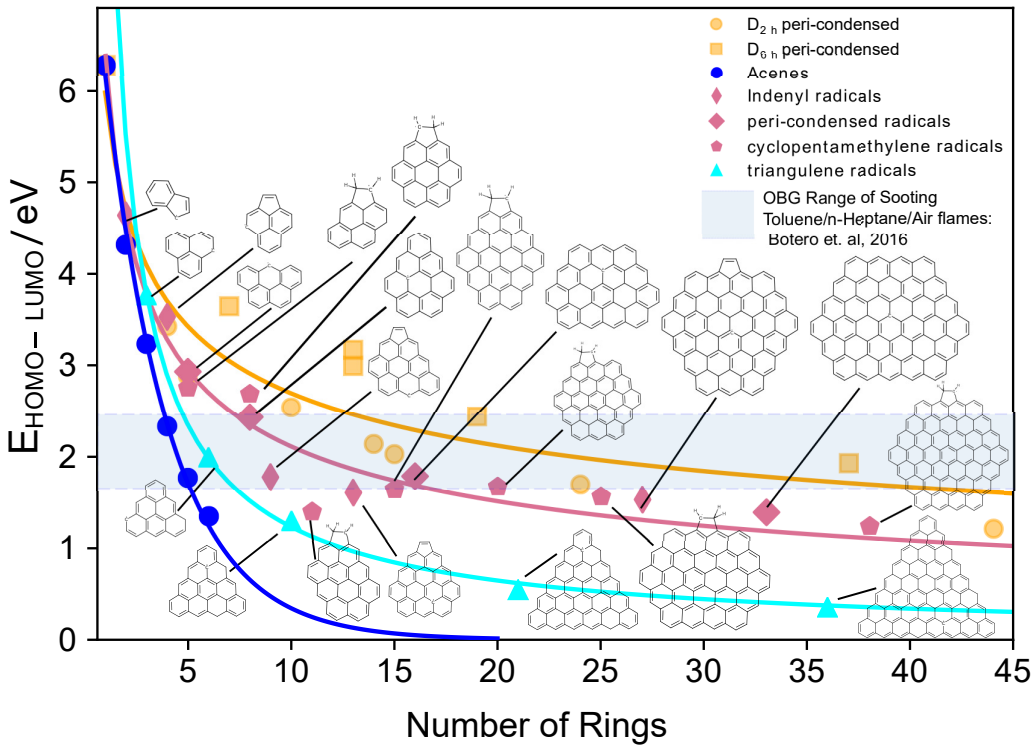

Figure 10: *Optical band gap of different resonance-stabilized-radical (RSR) PAHs as compared to closed-shell peri-condensed PAHs and acene series PAHs. The RSR PAHs include peri-condensed , indenyl-like , triangulene, and cyclopentamethylene RSR PAHs. The lines shown are power-law fittings, comparing the fits to all the peri-condensed flat PAHs calculated in section 3.2*

Figure 10 suggests that resonance-stabilized-radical PAHs have lower optical band gaps than closed-shell peri-condensed PAHs or their σ radicals on average. The triangulenes in particular have much lower OBGs than the other types of resonantly stabilized radicals. This is in spite of the fact that triangulenes have higher symmetry than the other π-radical PAHs and higher symmetry typically leads to larger OBG values. However, the triangulenes are also noted to typical possess bi-radical character as well as potential non-Kekulé structures that contribute to their energetics and optical properties as nano-graphene structures [55]. In the context of soot, triangulenes with OBG values in the range of 1.7 - 2.4 eV are expected to be very small, around 5-8 rings. Much like the acenes, these triangulenes are not expected to be very stable at flame temperatures. For the rest of the RSR PAHs, the size-range of PAHs that match the optical band gaps observed in sooting flames is significantly more narrow. At the upper end of 2.4 eV, the size of RSR PAHs is estimated to be $\approx$ 9 rings, significantly smaller than flat peri-condensed PAHs (12-13 rings), and curved peri-condensed PAHs ($\approx$ 16 rings). The lower end of 1.7 eV corresponds to a RSR PAH of size around 16 rings, suggesting that in general the RSR PAHs in soot would have to be smaller than other types of PAHs to explain the same OBG measurements. Given that such small PAHs are unlikely to be able to cluster physically, it would be expected that the RSR PAHs would need to cluster covalently to be stable, which is consistent with the recent hypothesis of Johansson *et al.* [29].

4 Conclusions

The accuracy of different functionals for Time-Dependent Density Functional Theory (TD-DFT) calculations of the optical band gap (OBG) of PAHs was evaluated by comparison with experimentally determined values. The results indicate that HSE06 gives the most accurate OBG values compared to other functionals, especially for smaller PAHs including cross-linked and curved PAHs. Certain popular hybrid functionals were seen to significantly overestimate the OBG due to being parametrised to give the transport gap. The HSE06 functional was further used for calculating the OBG of larger and more complex PAHs. The observed inverse power-law correlation of the OBG with number of rings was in agreement with previous reports. In case of homogeneous cross-linked PAHs, it was shown that orbital localization effects cause an asymptotic decrease in the OBG with increasing number of monomers. This effect was especially pronounced for larger PAH monomers. For cross-linking between two different PAHs, the OBG was shown to reflect the OBG of the largest monomer PAH and not the average of the monomers. The effect of PAH curvature was also studied by first comparing the OBG of peri-condensed curved PAHs with varying number of pentagons to the OBG of flat peri-condensed PAHs. These calculations suggested that PAH curvature is important when considering the higher value OBGs measured in flames, as curved PAHs are expected to be larger than flat ones for these higher OBG values. However, for lower OBG ranges or larger sizes, it was seen that flat and curved PAHs essentially converge to the same number, so this range cannot be explained by curvature effects. By inducing strain in corannulene, a small curved PAH, it was found that the difference in OBG between a flat corannulene and a highly strained corannulene is 0.4 eV, but there is a limit to how much curvature changes the OBG. This helped explain why larger flat and curved PAHs have similar OBG values. Finally, the effect of radical character on the OBG of PAHs was considered. σ-radical PAHs were seen to have the same OBG as their equivalent closed-shell structure, regardless of the location of the radical site as well. On the other hand, π-radical PAHs were seen to have significantly lower optical band gaps than flat peri-condensed species of the same size, meaning that smaller π-radicals may also be important PAHs to consider. Further steps would include considering the effects of clusters of curved PAHs and π-radical PAHs on the optical band gap, as well as understanding the kinetics and thermodynamics of the formation of larger curved and π-radical PAHs under flame conditions. The accuracy of different functionals for Time-Dependent Density Functional Theory (TD-DFT) calculations of the optical band gap (OBG) of PAHs was evaluated by comparison with experimentally determined values. The results indicate that HSE06 gives the most accurate OBG values compared to other functionals, especially for smaller PAHs including cross-linked and curved PAHs. Certain popular hybrid functionals were seen to significantly overestimate the OBG due to being parametrised to give the transport gap. The HSE06 functional was further used for calculating the OBG of larger and more complex PAHs. The observed inverse power-law correlation of the OBG with number of rings was in agreement with previous reports. In case of homogeneous cross-linked PAHs, it was shown that orbital localization effects cause an asymptotic decrease in the OBG with increasing number of monomers. This effect was especially pronounced for larger PAH monomers. For cross-linking between two different PAHs, the OBG was shown to reflect the OBG of the largest monomer PAH and not the average of the monomers. The effect

of PAH curvature was also studied by first comparing the OBG of peri-condensed curved PAHs with varying number of pentagons to the OBG of flat peri-condensed PAHs. These calculations suggested that PAH curvature is important when considering the higher value OBGs measured in flames, as curved PAHs are expected to be larger than flat ones for these higher OBG values. However, for lower OBG ranges or larger sizes, it was seen that flat and curved PAHs essentially converge to the same number, so this range cannot be explained by curvature effects. By inducing strain in corannulene, a small curved PAH, it was found that the difference in OBG between a flat corannulene and a highly strained corannulene is 0.4 eV, but there is a limit to how much curvature changes the OBG. This helped explain why larger flat and curved PAHs have similar OBG values. Finally, the effect of radical character on the OBG of PAHs was considered. σ-radical PAHs were seen to have the same OBG as their equivalent closed-shell structure, regardless of the location of the radical site as well. On the other hand, π-radical PAHs were seen to have significantly lower optical band gaps than flat peri-condensed species of the same size, meaning that smaller π-radicals may also be important PAHs to consider. Further steps would include considering the effects of clusters of curved PAHs and π-radical PAHs on the optical band gap, as well as understanding the kinetics and thermodynamics of the formation of larger curved and π-radical PAHs under flame conditions.

Acknowledgements

AM acknowledges Johnson Matthey for financial support. The authors also acknowledge the financial support of the Singapore National Research Foundation (NRF) through the Campus for Research Excellence and Technological Enterprise (CREATE) program. MK gratefully acknowledges the support of the Alexander von Humboldt foundation.

Supplementary Material

One file of supplementary material is available for this paper. The supplementary material includes structures, characteristics, and OBG values for the 19 PAHs studied both experimentally and using TD-DFT. Details on the UV/Visible spectroscopy methods, constrained geometry optimizations, and aromatic fluctuation index calculations are also provided.

Appendix

The structures of the 19 molecules whose OBG was measured experimentally by UV-Visible spectroscopy are are displayed in Fig. S1. Properties of these PAHs and the supplier are detailed in Table 1 below. The measured and calculated optical band gaps are also provided in Table 2.

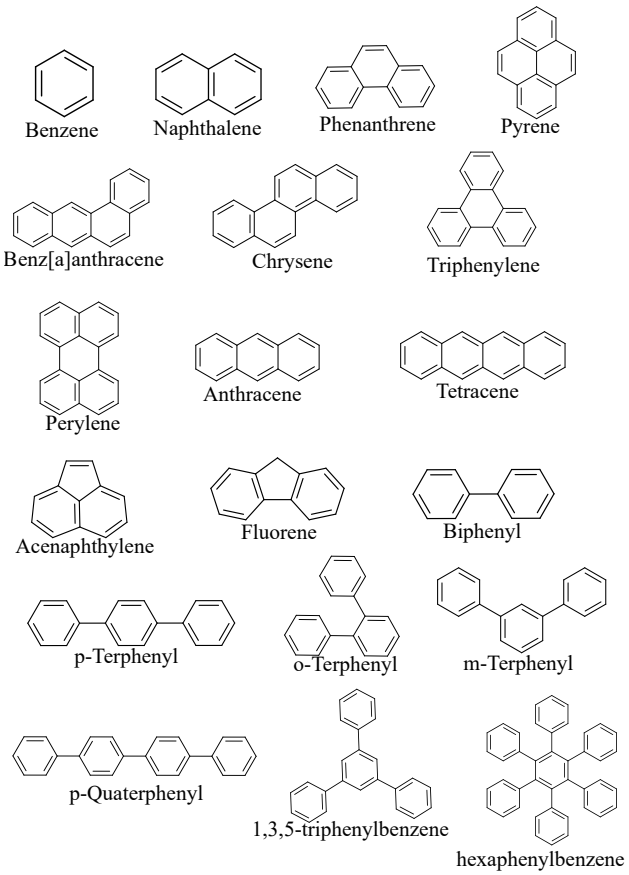

Figure S1: *Structures of the 19 molecules studied both experimentally and computationally in the main paper.*

Table 1: *List of PAHs studied experimentally in this work and their properties.*

Species	Number of Rings	$\frac{C}{H}$ ratio	Category	Supplier
Benzene	1	1.0	N/A	TCI
Naphthalene	2	1.25	Peri-Condensed/Acene	Sigma Aldrich
Phenanthrene	3	1.4	Peri-Condensed	Sigma Aldrich
Pyrene	4	1.6	Peri-Condensed	Sigma Aldrich
Benz[a]anthracene	4	1.5	Peri-Condensed	TCI
Chrysene	4	1.5	Peri-Condensed	TCI
Triphenylene	4	1.5	Peri-Condensed	Sigma Aldrich
Perylene	5	1.67	Peri-Condensed	TCI
Anthracene	3	1.4	Acene	Acros
Tetracene	4	1.5	Acene	Acros
Acenaphthylene	3(1 pentagonal)	1.5	Pentagonal	Sigma Aldrich
Fluorene	3(1 pentagonal)	1.3	Pentagonal	Sigma Aldrich
Biphenyl	2	1.2	Cross-linked	TCI
p-Terphenyl	3	1.29	Cross-linked	TCI
m-Terphenyl	3	1.29	Cross-linked	TCI
o-Terphenyl	3	1.29	Cross-linked	TCI
p-Quaterphenyl	4	1.33	Cross-linked	TCI
1,3,5-Triphenylbenzene	4	1.33	Cross-linked	Sigma Aldrich
Hexaphenylbenzene	6	1.4	Cross-linked	Sigma Aldrich

Table 2: *Experimental and TD-DFT Band Gaps, HOMO energies, and LUMO energies.*

Species	$E_{g,\mathrm{Exp}}$	$E_{g,\mathrm{DFT}}$	E_{LUMO}	E_{HOMO}
Benzene	5.79	6.28	-0.64	-6.92
Naphthalene	4.22	4.31	-1.57	-5.88
Phenanthrene	4.16	4.02	-1.74	-5.76
Pyrene	3.64	3.42	-2.07	-5.49
Benz[a]anthracene	3.34	3.34	-2.08	-5.43
Chrysene	3.80	3.84	-1.79	-5.63
Triphenylene	4.10	4.43	-1.50	-5.93
Perylene	2.79	2.89	-2.53	-5.41
Anthracene	3.27	3.23	-2.11	-5.34
Tetracene	2.63	2.33	-2.68	-5.01
Acenaphthylene	3.59	3.68	-2.38	-6.06
Fluorene	4.06	4.33	-1.36	-5.68
Biphenyl	4.44	4.94	-1.20	-6.05
p-Terphenyl	4.00	4.32	-1.65	-5.97
m-Terphenyl	4.43	4.69	-1.46	-6.15
o-Terphenyl	4.21	4.68	-1.33	-6.01
p-Quaterphenyl	3.79	4.01	-1.81	-5.83
1,3,5-Triphenylbenzene	4.35	4.55	-1.50	-6.05
Hexaphenylbenzene	4.14	4.45	-1.58	-6.02

Determining Optical Band Gaps from UV/Visible Spectroscopy

We determine the optical band gap from UV/Visible spectroscopy using the absorption edge method as detailed in other works [10, 11, 14]. The peak of the low absorption band is located and then extrapolation is performed to locate the absorption edge, the point at which the absorption starts to occur, by finding the intersection between the baseline and the slope determined from the low absorption band maximum. This wavelength is then converted to the optical band gap using the standard formula:

$$E_g = \frac{1240}{\lambda_{\mathrm{a.e}}}. \tag{4.2}$$

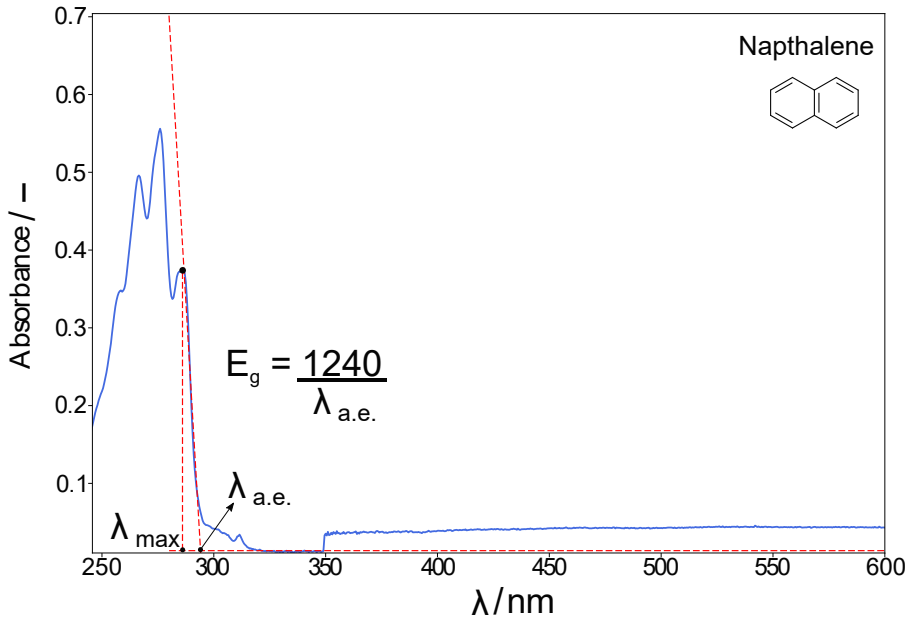

Figure S2: *Example plot of absorbance against wavelength spectra for naphthalene zoomed in on the low energy absorption band. The method for determining the wavelength at the absorption edge is illustrated, along with the method of extrapolation.*

The baseline value changes at 350 nm due to the change in light source from Visible to UV. The baseline value is taken as the baseline just before the absorption starts to occur. There is some noise present in the baseline prior to the start of the absorption, so an average is taken for the baseline value before absorption occurs.

Constrained Geometry Optimization of Corannulene

As mentioned in the main text, the curvature of corannulene was altered artificially by fixing the values of the internal dihedral angles between the pentagonal and the hexagonal planes in the molecule, as done in Martin et al [31]. This is illustrated in Fig S3 below:

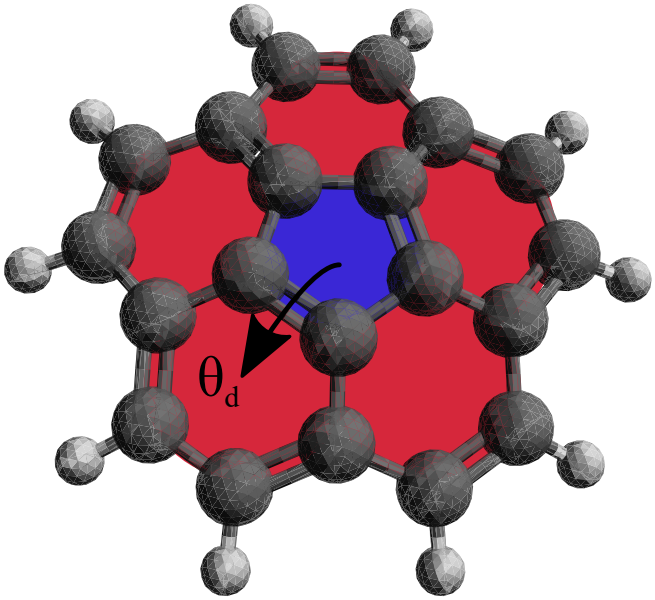

Figure S3: *Top view of Corannulene molecule. The internal dihedral angles that are constrained during the geometry optimization are the angles between the pentagon (shaded in blue) and the hexagons (shaded in red).*

The dihedral angle, θ_d, of corannulene from an unconstrained optimization using the B3LYP/6-311G** level of theory is 152.6°. θ_d was varied between 140°, representing a strained corannulene that is more curved than the normal conformer, and 180°, which represents a corannulene that has been restricted to be entirely planar.

Calculation of Aromatic Fluctuation Index

The aromatic fluctuation index (FLU) is defined in Matito et al. [37]. It is an aromatic index based on electron delocalization and has advantages over other commonly used aromaticity indices such as para-delocalization index (PDI) in that it can be applied to study non-6-membered rings as well. The FLU is calculated as follows:

$$\mathrm{FLU} = \frac{1}{n}\sum_{R}\left[\left(\frac{V(B)}{V(A)}\right)^{(V(B)-V(A))}\left(\frac{\delta(A,B)-\delta_{ref}(A,B)}{\delta_{ref}(A,B)}\right)\right]^2$$

$$R = \{A-B \mid A,B \text{ are neighbours in Ring-R}\}$$

The summation is taken over all adjacent pairs of carbon atoms, (A,B), when traversing the ring, R. V represents the valency of the atom, in question, δ is the delocalization of electrons for the C-C atom-pair, and δ_{ref} is the reference delocalization value as calculated for benzene,. A lower value of FLU therefore indicates a more aromatic ring. The calculations FLU for the rings in fluorene and acenaphthylene were performed using

the Multiwfn program suite [35]. The FLU for the pentagonal ring in fluorene is 0.050 compared to 0.040 for acenaphthylene. This firstly suggests that the pentagon in acenaphthylene is more aromatic than the pentagon in fluorene, which would agree with their respective structures as the pentagon in fluorene is not fully delocalized. In addition, these values of FLU for the pentagons would suggest low aromaticity of the five-membered ring in both fluorene and acenaphthylene. The FLU for the hexagonal rings in fluorene is 0.003 compared to 0.013 for the hexagonal rings in acenaphthylene. This suggests that the hexagonal rings in fluorene are more aromatic than those for acenaphthylene. In this case, the pentagonal rings in both molecules are not very aromatic. However, the hexagonal rings in fluorene are quite aromatic, and significantly more so than the hexagonal rings in acenaphthylene. This would suggest that fluorene is more aromatic than acenaphthylene, which could explain it having a significantly higher OBG.

Structures of PAHs studied

The molecular structures of the acenes and peri-condensed PAHs in Figures 3 and 9 are displayed in Figure S4. The molecular structures of the cross-linked PAHs in Figure 5 are displayed in Figure S5 and the curved PAHs in Figure 7 are displayed in Figure S6. The molecular structures of the various resonantly-stabilized-radical PAHs in Figure 10 are displayed in Figure S7.

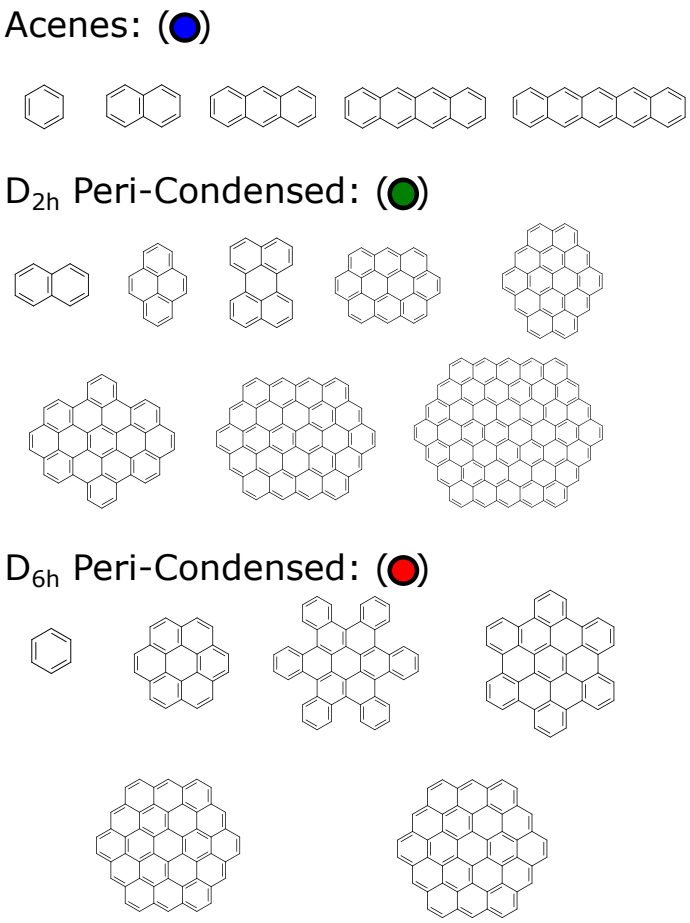

Figure S4: *Molecular structures of the flat PAHs studied in this work, divided into acenes, D_{2h} PAHs, and D_{6h} PAHs.*

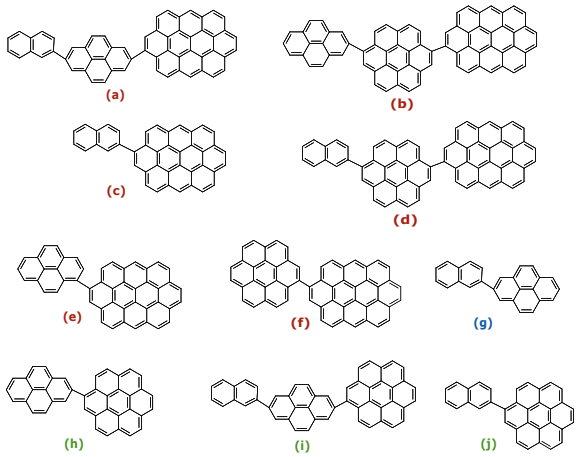

Figure S5: *Molecular structures of the cross-linked PAHs consisting of different monomers studied in this work. Lettering and coloring matches with Figure 4a in the main article.*

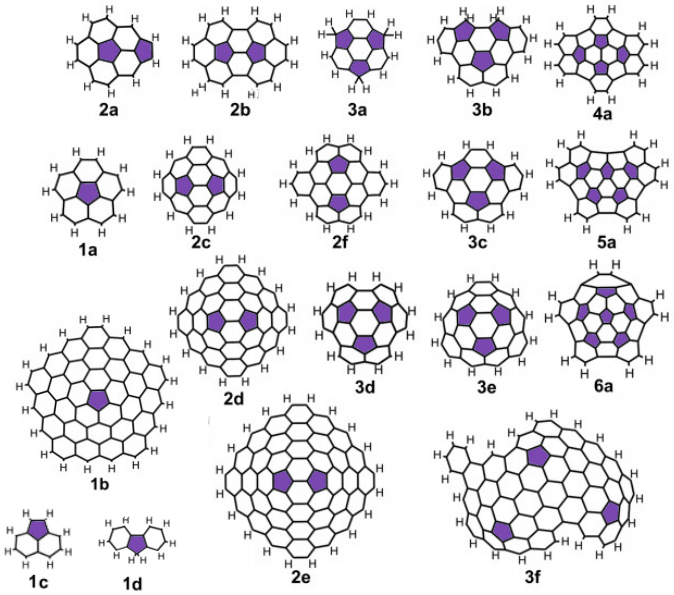

Figure S6: *Molecular structures of the curved PAHs studied in this work. The number indicates the number of pentagons in the molecule and the lettering is to be consistent with [31]. Pentagons are shaded purple for clarity.*

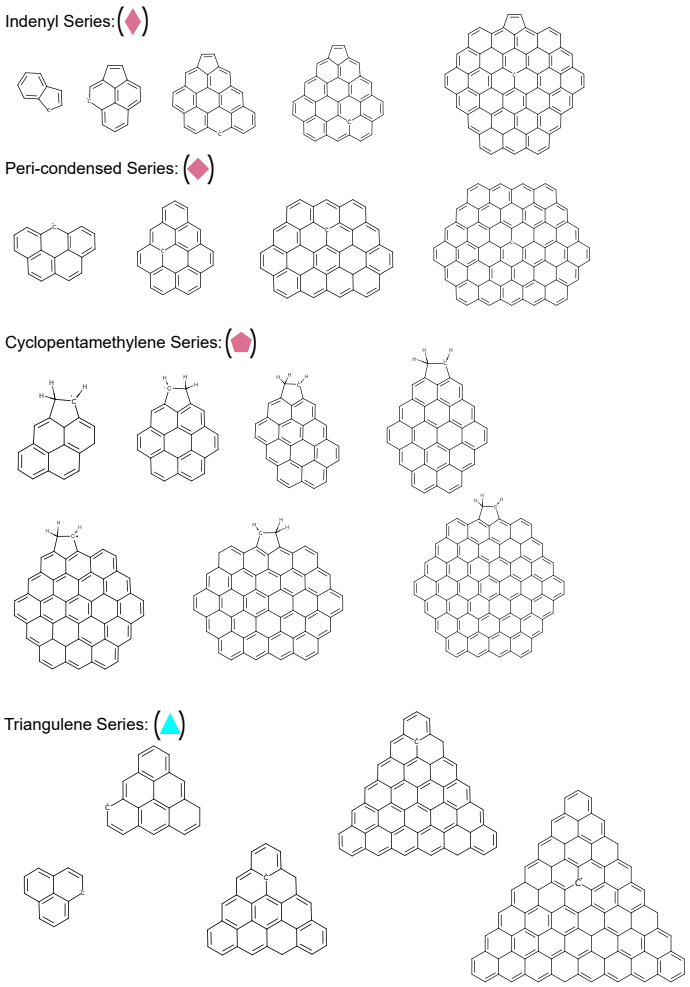

Figure S7: *Molecular structures of the resonance-stabilized-radical PAHs studied in this work, categorized into the 4 main types.*

References

[1] Polar curved polycyclic aromatic hydrocarbons in soot formation. *Proceedings of the Combustion Institute*, 37(1):1117 – 1123, 2019. ISSN 1540-7489. doi:https://doi.org/10.1016/j.proci.2018.05.046.

[2] H.X. Chen, R.A. Dobbins. Crystallogenesis of particles formed in hydrocarbon combustion. *Combust. Sci. Technol.*, 159(1):109–128, 2000. doi:10.1080/00102200008935779.

[3] A. D'Alessio, A. D'Anna, G. Gambi, P. Minutolo. The optical band gap model in the interpretation of the UV-visible absorption spectra of rich premixed flames. *Symposium (International) on Combustion*, 26(1):951–957, 1996. doi:10.1016/S0082-0784(96)80307-9.

[4] A.C. Ferrari, J. Robertson. Interpretation of Raman spectra of disordered and amorphous carbon. *Phys. Rev. B*, 61(20):14095–14107, 2000. doi:10.1103/PhysRevB.61.14095.

[5] A.D. Zdetsis, E.N. Economou. Interrelation of aromaticity and conductivity of graphene dots/antidots and related nanostructures. *J. Phys. Chem. C*, 120(51): 29463–29475, 2016. doi:10.1021/acs.jpcc.6b09532.

[6] A.L. Lafleur, J.B. Howard, J.A. Marr, T. Yapesh. Proposed fullerene precursor corannulene identified in flames both in the presence and absence of fullerene production. *J. Phys. Chem. C.*, 97(51):13539–13543, 1993. doi:10.1021/j100153a020.

[7] R. Andreu, J. Garín, and J. Orduna. Electronic absorption spectra of closed and open-shell tetrathiafulvalenes: the first time-dependent density-functional study. *Tetrahedron*, 57(37):7883 – 7892, 2001. doi:https://doi.org/10.1016/S0040-4020(01)00766-9.

[8] P. Avouris. Molecular electronics with carbon nanotubes. *Accounts Chem. Res.*, 35 (12):1026–1034, 2002. doi:10.1021/ar010152e.

[9] M. Bachmann, W. Wiese, and K.-H. Homann. PAH and aromers: Precursors of fullerenes and soot. *Symposium (International) on Combustion*, 26(2):2259 – 2267, 1996. ISSN 0082-0784. doi:https://doi.org/10.1016/S0082-0784(96)80053-1.

[10] A. S. Bhadwal, R. M. Tripathi, R. K. Gupta, N. Kumar, R. P. Singh, and A. Shrivastav. Biogenic synthesis and photocatalytic activity of cds nanoparticles. *RSC Adv.*, 4:9484–9490, 2014. doi:10.1039/C3RA46221H.

[11] Y. Caglar, S. Ilican, and M. Caglar. Single-oscillator model and determination of optical constants of spray pyrolyzed amorphous sno2 thin films. *Eur. Phys. J. B.*, 58 (3):251–256, Aug 2007. doi:10.1140/epjb/e2007-00227-y.

[12] D. Chen, T. S. Totton, J. W. Akroyd, S. Mosbach, and M. Kraft. Size-dependent melting of polycyclic aromatic hydrocarbon nano-clusters: A molecular dynamics study. *Carbon*, 67(Supplement C):79 – 91, 2014. doi:https://doi.org/10.1016/j.carbon.2013.09.058.

[13] S. J. Clark and J. Robertson. Screened exchange density functional applied to solids. *Phys. Rev. B*, 82:085–208, Aug 2010. doi:10.1103/PhysRevB.82.085208.

[14] J. C. Costa, R. J. Taveira, C. F. Lima, A. Mendes, and L. M. Santos. Optical band gaps of organic semiconductor materials. *Opt. Mater.*, 58(Supplement C):51 – 60, 2016. doi:https://doi.org/10.1016/j.optmat.2016.03.041.

[15] P. Elvati and A. Violi. Thermodynamics of poly-aromatic hydrocarbon clustering and the effects of substituted aliphatic chains. *P. Combust. Inst.*, 34(1):1837 – 1843, 2013. doi:https://doi.org/10.1016/j.proci.2012.07.030.

[16] E.M. Adkins, J.A. Giaccai, J.H. Miller. Computed electronic structure of polynuclear aromatic hydrocarbon agglomerates. *P. Combust. Inst.*, 36(1):957 – 964, 2017. doi:https://doi.org/10.1016/j.proci.2016.06.186.

[17] E.M. Adkins, J.H. Miller. Extinction measurements for optical band gap determination of soot in a series of nitrogen-diluted ethylene/air non-premixed flames. *Phys. Chem. Chem. Phys.*, 17(4):2686–2695, 2015. doi:10.1039/C4CP04452E.

[18] E.M. Adkins, J.H. Miller. Towards a taxonomy of topology for polynuclear aromatic hydrocarbons: linking electronic and molecular structure. *Phys. Chem. Chem. Phys.*, 19:28458–28469, 2017. doi:10.1039/C7CP06048C.

[19] M. Ezawa. Metallic graphene nanodisks: Electronic and magnetic properties. *Phys. Rev. B*, 76:245415, Dec 2007. doi:10.1103/PhysRevB.76.245415.

[20] M. Frenklach. Reaction mechanism of soot formation in flames. *Phys. Chem. Chem. Phys.*, 4:2028–2037, 2002. doi:10.1039/B110045A.

[21] M. Frenklach. New form for reduced modeling of soot oxidation: Accounting for multi-site kinetics and surface reactivity. *Combustion and Flame*, 201:148 – 159, 2019. ISSN 0010-2180. doi:https://doi.org/10.1016/j.combustflame.2018.12.023.

[22] H. Wang, M. Frenklach. A detailed kinetic modeling study of aromatics formation in laminar premixed acetylene and ethylene flames. *Combust. Flame*, 110(1):173 – 221, 1997. doi:10.1016/S0010-2180(97)00068-0.

[23] K.-H. Homann. Fullerenes and soot formation - new pathways to large particles in flames. *Angewandte Chemie International Edition*, 37(18): 2434–2451, 1998. doi:10.1002/(SICI)1521-3773(19981002)37:18<2434::AID-ANIE2434>3.0.CO;2-L.

[24] J. B. Howard. Carbon addition and oxidation reactions in heterogeneous combustion and soot formation. *Symposium (International) on Combustion*, 23(1):1107 – 1127, 1991. ISSN 0082-0784. doi:https://doi.org/10.1016/S0082-0784(06)80371-1. Twenty-Third Symposium (International) on Combustion.

[25] J. Robertson, E. O'Reilly. Electronic and atomic structure of amorphous carbon. *Phys. Rev. B*, 35(6):2946–2957, 1987. doi:10.1103/PhysRevB.35.2946.

[26] J. Tauc, R. Grigorovici, A. Vancu. Optical Properties and Electronic Structure of Amorphous Germanium. *Phys. Status Solidi (B)*, 15(2):627–637, 1966. doi:10.1002/pssb.19660150224.

[27] C. Jäger, F. Huisken, H. Mutschke, I. L. Jansa, and T. Henning. Formation of Polycyclic Aromatic Hydrocarbons and Carbonaceous Solids in Gas-Phase Condensation Experiments. *Astrophys. J.*, 696:706–712, May 2009. doi:10.1088/0004-637X/696/1/706.

[28] J.D. Herdman, J.H. Miller. Intermolecular potential calculations for polynuclear aromatic hydrocarbon clusters. *J. Phys. Chem. A*, 112(28):6249–6256, 2008. doi:10.1021/jp800483h.

[29] K. Johansson, M. Head-Gordon, P. Schrader, K. Wilson, and H. Michelsen. Resonance-stabilized hydrocarbon-radical chain reactions may explain soot inception and growth. *Science*, 361(6406):997–1000, 2018.

[30] J.W. Martin, G.J. McIntosh, R. Arul, R.N. Oosterbeek, M. Kraft, T. Söhnel. Giant fullerene formation through thermal treatment of fullerene soot. *Carbon*, 125:132–138, dec 2017. doi:10.1016/j.carbon.2017.09.045.

[31] J.W. Martin, R.I. Slavchov, E.K.Y Yapp, J. Akroyd, S. Mosbach, M. Kraft. The polarization of polycyclic aromatic hydrocarbons curved by pentagon incorporation: The role of the flexoelectric dipole. *J. Phys. Chem. C.*, 0(ja), 2017. doi:10.1021/acs.jpcc.7b09044.

[32] P. Lavvas, M. Sander, M. Kraft, and H. Imanaka. Surface chemistry and particle shape: processes for the evolution of aerosols in titan's atmosphere. *The Astrophysical Journal*, 728(2):80, 2011.

[33] P. Liu, Z. Li, A. Bennett, H. Lin, S. M. Sarathy, and W. L. Roberts. The site effect on PAHs formation in HACA-based mass growth process. *Combustion and Flame*, 199:54 – 68, 2019. ISSN 0010-2180. doi:https://doi.org/10.1016/j.combustflame.2018.10.010.

[34] J. S. Lowe, J. Y. Lai, P. Elvati, and A. Violi. Towards a predictive model for polycyclic aromatic hydrocarbon dimerization propensity. *P. Combust. Inst.*, 35(2):1827 – 1832, 2015. doi:https://doi.org/10.1016/j.proci.2014.06.142.

[35] T. Lu and F. Chen. Multiwfn: A multifunctional wavefunction analyzer. *J. Comput. Chem.*, 33(5):580–592, 2012. doi:10.1002/jcc.22885.

[36] Q. Mao, A. C. van Duin, and K. Luo. Formation of incipient soot particles from polycyclic aromatic hydrocarbons: A ReaxFF molecular dynamics study. *Carbon*, 121:380 – 388, 2017. ISSN 0008-6223. doi:https://doi.org/10.1016/j.carbon.2017.06.009.

[37] E. Matito, M. Duran, and M. Sola. The aromatic fluctuation index (flu): A new aromaticity index based on electron delocalization. *J. Chem. Phys.*, 122(1):014109, 2005. doi:10.1063/1.1824895.

[38] A. M. Mebel and R. I. Kaiser. Formation of resonantly stabilised free radicals via the reactions of atomic carbon, dicarbon, and tricarbon with unsaturated hydrocarbons: theory and crossed molecular beams experiments. *International Reviews in Physical Chemistry*, 34(4):461–514, 2015. doi:10.1080/0144235X.2015.1075280.

[39] M.J. Frisch, G.W. Trucks, H.B. Schlegel, G.E. Scuseria, M.A. Robb, J.R. Cheeseman, G. Scalmani, V. Barone, B. Mennucci, G.A. Petersson, H. Nakatsuji et al. Gaussian 09 revision d.1, 2009. Gaussian Inc. Wallingford CT 2009.

[40] M.J. Frisch, G.W. Trucks,H.B. Schlegel, G.E. Scuseria, M.A. Robb, J.R. Cheeseman , J.A. Montgomery, T. Vreven, K.N. Kudin, J.C. Burant, J.M. Millam, S.S. Iyengar, J. Tomasi, V. Barone et al. Gaussian 03, Revision C.02, 2004. Gaussian, Inc., Wallingford, CT, 2004.

[41] M.L. Botero, E.M. Adkins, S. Gonzalez-Calera, J.H. Miller, M. Kraft. PAH structure analysis of soot in a non-premixed flame using high-resolution transmission electron microscopy and optical band gap analysis. *Combust. Flame*, 164:250–258, 2016. doi:10.1016/j.combustflame.2015.11.022.

[42] J. A. Plumley and J. J. Dannenberg. A comparison of the behavior of functional/basis set combinations for hydrogen-bonding in the water dimer with emphasis on basis set superposition error. *J. Comp. Chem.*, 2011. doi:10.1002/jcc.21729.

[43] H. Richter and J. Howard. Formation of polycyclic aromatic hydrocarbons and their growth to soot-a review of chemical reaction pathways. *Progress in Energy and Combustion Science*, 26(4):565 – 608, 2000. doi:https://doi.org/10.1016/S0360-1285(00)00009-5.

[44] Y. Ruiz-Morales. HOMO-LUMO gap as an index of molecular size and structure for polycyclic aromatic hydrocarbons (pahs) and asphaltenes: A theoretical study. I. *J. Phys. Chem. A.*, 106(46):11283–11308, 2002. doi:10.1021/jp021152e.

[45] U. Salzner and A. Aydin. Improved prediction of properties of -conjugated oligomers with range-separated hybrid density functionals. *J. Chem. Theory Comput.*, 7(8):2568–2583, 2011. doi:10.1021/ct2003447.

[46] F. Schulz, M. Commodo, K. Kaiser, G. D. Falco, P. Minutolo, G. Meyer, A. D'Anna, and L. Gross. Insights into incipient soot formation by atomic force microscopy. *Proceedings of the Combustion Institute*, 37(1):885 – 892, 2019. ISSN 1540-7489. doi:https://doi.org/10.1016/j.proci.2018.06.100.

[47] R. Singh and M. Frenklach. A mechanistic study of the influence of graphene curvature on the rate of high-temperature oxidation by molecular oxygen. *Carbon*, 101: 203 – 212, 2016. doi:https://doi.org/10.1016/j.carbon.2016.01.090.

[48] S. Sinha and A. Raj. Polycyclic aromatic hydrocarbon (pah) formation from benzyl radicals: a reaction kinetics study. *Phys. Chem. Chem. Phys.*, 18:8120–8131, 2016. doi:10.1039/C5CP06465A.

[49] S. Stein. On the high temperature chemical equilibria of polycyclic aromatic hydrocarbons. *The Journal of Physical Chemistry*, 82(5):566–571, 1978. doi:10.1021/j100494a600.

[50] A. G. Tielens. Interstellar polycyclic aromatic hydrocarbon molecules. *Annu. Rev. Astron. Astrophys.*, 46:289–337, 2008.

[51] T.S. Totton, A.J. Misquitta, M. Kraft. A quantitative study of the clustering of polycyclic aromatic hydrocarbons at high temperatures. *Phys. Chem. Chem. Phys.*, 14 (12):4081, 2012. doi:10.1039/c2cp23008a.

[52] H. Wang. Formation of nascent soot and other condensed-phase materials in flames. *Proceedings of the Combustion Institute*, 33(1):41–67, 2011. doi:10.1016/j.proci.2010.09.009.

[53] E. K. Yapp, R. I. Patterson, J. Akroyd, S. Mosbach, E. M. Adkins, J. H. Miller, and M. Kraft. Numerical simulation and parametric sensitivity study of optical band gap in a laminar co-flow ethylene diffusion flame. *Combust. Flame*, 167:320 – 334, 2016. doi:https://doi.org/10.1016/j.combustflame.2016.01.033.

[54] E. K. Y. Yapp and M. Kraft. *Modelling Soot Formation: Model of Particle Formation*, pages 389–407. Springer London, London, 2013.

[55] C.-N. Yeh and J.-D. Chai. Role of kekulé and non-kekulé structures in the radical character of alternant polycyclic aromatic hydrocarbons: a tao-dft study. *Scientific reports*, 6:30562, 2016.

[56] A. V. Zabula, A. S. Filatov, S. N. Spisak, A. Y. Rogachev, and M. A. Petrukhina. A main group metal sandwich: Five lithium cations jammed between two corannulene tetraanion decks. *Science*, 333(6045):1008–1011, 2011. doi:10.1126/science.1208686.

[57] F. Zhang, R. Wang, Y. Wang, X. Zhang, and B. Liu. Targeted and selective HOMO energy control by fine regulation of molecular planarity and its effect on the interfacial charge transfer process in dye-sensitized solar cells. *Phys. Chem. Chem. Phys.*, pages –, 2019. doi:10.1039/C9CP00091G.

[58] L. Zhao, R. I. Kaiser, B. Xu, U. Ablikim, M. Ahmed, M. M. Evseev, E. K. Bashkirov, V. N. Azyazov, and A. M. Mebel. Low-temperature formation of polycyclic aromatic hydrocarbons in titan's atmosphere. *Nature Astronomy*, 2(12):973, 2018.